

Plasmonic Metasurface Resonators to Enhance Terahertz Magnetic Fields for High-Frequency Electron Paramagnetic Resonance

Lorenzo Tesi,* Dominik Bloos, Martin Hrtoň, Adam Beneš, Mario Hentschel, Michal Kern, Alisa Leavesley, Rainer Hillenbrand, Vlastimil Křápek, Tomáš Šíkola, and Joris van Slageren*

Nanoscale magnetic systems play a decisive role in areas ranging from biology to spintronics. Although, in principle, THz electron paramagnetic resonance (EPR) provides high-resolution access to their properties, lack of sensitivity has precluded realizing this potential. To resolve this issue, the principle of plasmonic enhancement of electromagnetic fields that is used in electric dipole spectroscopies with great success is exploited, and a new type of resonators for the enhancement of THz magnetic fields in a microscopic volume is proposed. A resonator composed of an array of diabolical antennas with a back-reflecting mirror is designed and fabricated. Simulations and THz EPR measurements demonstrate a 30-fold signal increase for thin film samples. This enhancement factor increases to a theoretical value of 7500 for samples confined to the active region of the antennas. These findings open the door to the elucidation of fundamental processes in nanoscale samples, including junctions in spintronic devices or biological membranes.

integer-spin species with large zero-field splittings,^[3] there has been a drive toward employing higher magnetic fields and microwave frequencies. This transition was started from the conventional X-band (i.e., 300 mT and 9 GHz) and has reached THz frequencies, where magnetic fields above 5 T and frequencies higher than about 100 GHz are used.^[4] Nowadays, high-frequency EPR (HFEPR) instruments operate in a broad frequency range, from 100 GHz up to about 1 THz, and further improvements can be expected to emerge from recent THz technological developments.^[5,6] A key element of any conventional EPR instrument is the resonator, which is commonly a 3D cavity that enhances the microwave magnetic field in a specific volume, thus increasing

1. Introduction

Electron paramagnetic resonance (EPR) spectroscopy is a well-established technique for investigating systems with unpaired electrons. It is widely applied in research areas including chemistry, physics, medicine, biology, and materials science.^[1,2] To enhance absolute sensitivity, spectral resolution and access

the measurement sensitivity. Single-mode cavities are the most used resonators but, since their dimensions scale with the third power of the wavelength, they are too small for use in HFEPR.^[1] 3D Fabry–Pérot resonators are more amenable to high-frequency applications; however, their employment is limited by drawbacks such as high resistive losses and low filling factors.^[1,7] For these reasons, and because bulk samples often


L. Tesi, D. Bloos, A. Beneš, M. Kern, J. van Slageren
Institute of Physical Chemistry and Center for Integrated Quantum Science and Technology
University of Stuttgart
D-70569 Stuttgart, Germany
E-mail: lorenzo.tesi@ipc.uni-stuttgart.de; slageren@ipc.uni-stuttgart.de
M. Hrtoň, V. Křápek, T. Šíkola
Institute of Physical Engineering and Central European Institute of Technology
Brno University of Technology
Brno 616 69, Czech Republic

M. Hentschel
4th Physics Institute and Research Center SCoPE
University of Stuttgart
D-70569 Stuttgart, Germany

A. Leavesley
Thomas Keating Ltd.
Billingshurst RH14 9SH, UK

R. Hillenbrand
IKERBASQUE
Basque Foundation for Science
Bilbao 48013, Spain

R. Hillenbrand
CIC nanoGune BRTA and Department of Electricity and Electronics UPV/EHU
Donostia-San Sebastián 20018, Spain

 The ORCID identification number(s) for the author(s) of this article can be found under <https://doi.org/10.1002/smt.202100376>.

© 2021 The Authors. Small Methods published by Wiley-VCH GmbH. This is an open access article under the terms of the Creative Commons Attribution License, which permits use, distribution and reproduction in any medium, provided the original work is properly cited.

DOI: 10.1002/smt.202100376

give strong signals, HFEPR measurements are typically carried out without any resonator. However, this is no longer viable when dealing with volume-limited samples, ranging from biochemical materials to thin magnetic layers. To underline the importance of accessing information from volume-limited samples, we provide here a few practical examples. EPR is used to investigate the conformation and dynamics of enzymes via spin-labeling methods, which allows for the elucidation of the mechanisms of enzyme functioning.^[8,9] However, the preparation of large quantities of spin-labeled biomolecules is usually prohibitively challenging. Moreover, self-assembled monolayers of biomolecules are used in combination with nanoparticles for drug-delivery systems,^[10] and for progress in this area it is fundamental to improve the tools for their characterization. In the context of thin magnetic layers, two examples of topical molecular magnetic materials are single-molecule magnets, for realizing nanomagnetic data storage, and molecular spin qubits, for implementing quantum technologies.^[11–15] The properties of these molecular systems are also appealing for realizing spintronic devices, which requires their deposition and characterization onto surfaces.^[16–18] However, the changes of their properties, as compared to the bulk material, following deposition onto a surface are still poorly understood and their study is essentially limited to synchrotron techniques.^[19,20] Although synchrotron methods allow for the investigation of relevant properties, they cannot be used for physical addressing of these materials, which is a requirement for the progress in molecular quantum spintronic devices. The development of more sensitive techniques for studying and addressing species in a monolayer or thin films is clearly warranted and 3D resonator schemes are insufficient for this purpose. Indeed, when this type of sample is placed in a 3D resonator it fills only a very small fraction of the mode volume, leading to very small signal intensities. In this respect, 2D resonators are a promising alternative.

Single 2D microresonators in the microwave frequency range (2–15 GHz) for EPR have been previously investigated with increased sensitivities by more than one order of magnitude.^[21–26] In contrast, 2D resonators operating in the THz frequency region have not yet been reported. 2D resonators at conventional microwave frequencies are single entities that employ coplanar waveguides or strip-lines to couple the radiation into the resonator. The use of waveguides is not convenient at THz frequencies since losses through them are prohibitive. Thus, quasi-optical, free-space methods must be employed. Free-space coupling has the additional advantage that many resonators can be easily coupled to the same radiation source. A conceptual way to realize THz planar resonators and their coupling to THz electromagnetic radiation is by exploiting the unique properties of plasmonic metasurfaces.^[27] In general, metamaterials are artificial materials composed of periodic arrays of subwavelength plasmonic units with a specifically tailored electromagnetic response that goes beyond what is found in nature.^[28–30] Metasurfaces are metamaterials with subwavelength thickness.^[31,32] Their electromagnetic response can be derived either from the effect of individual plasmonic resonators or plasmonic antennas (PAs), or from the propagation of surface plasmons involving the entire array structure.^[33,34] The nature of the response depends on the shape and dimensions of the plasmonic units and their configuration. This allows for tailoring the metasurface properties depending on the specific

application.^[35–37] Here, we are interested in the capability of squeezing the electromagnetic radiation beyond the diffraction limit, in a similar fashion to the use of nanoantennas in visible and near-infrared frequencies that led to a sensitivity revolution.^[38] This striking sensitivity was exploited in a range of techniques, e.g., Raman spectroscopy,^[39,40] fluorescence,^[41] photocatalysis,^[42] magneto-optics,^[43] biosensing,^[44,45] etc.^[46–48] In our case, we aim to focus THz electromagnetic radiation in a subwavelength volume to enhance the *magnetic* field of the radiation, consequently increasing the sensitivity of HFEPR spectroscopy when measuring thin layers and nanostructured samples. Therefore, in this work we design, fabricate, and characterize a plasmonic metasurface resonator (PMR) based on diablo PA. We show HFEPR measurements of a magnetic thin film deposited on the PMR and find signal enhancements of a factor of 30 averaged over the entire thin layer sample, which is estimated to be a factor of 7500 when considering only the area above the PAs. The manuscript is organized as follows: First, we discuss the simulations of the PMR and assess the effect of the individual components on the total response. Second, we describe the characterization of the fabricated PMR by THz transmission and double-transmission experiments, together with the respective simulations. Then, we present the HFEPR experimental results with and without the use of the PMR. Finally, we discuss the potential signal enhancement from the PMR for specific but highly relevant cases.

2. Results

2.1. Design of the Resonator

The concept of the experiment is depicted in **Figure 1**. To translate the concept to working principles, the design of the PMR follows from six main criteria that we identified as fundamental for high-sensitivity applications in HFEPR spectroscopy. These criteria are outlined in the following. 1) Frequency: the geometric dimensions of the plasmonic units must be adjusted to match the desired resonance frequency. 2) Bandwidth: conventional EPR operates in field-domain, i.e., the external DC magnetic field (B_0) is swept at constant microwave frequencies (B_1). In this case, a narrow frequency bandwidth, corresponding to a stronger field intensity, is preferred. 3) B_1 orientation: in EPR, the magnetic field of the radiation, B_1 , must be perpendicular to the external DC magnetic field B_0 . Depending on the geometry of the magnet that is used to produce B_0 , it may be preferable to use PAs that produce magnetic fields oriented in the plane of or normal to the array. 4) Polarization of the incident electromagnetic radiation: the response of PAs depends on this orientation. This feature can be used as a switch of the PMR response and to produce a specific polarization of the electromagnetic radiation. 5) Spatial extension of the PAs resonance mode: for extended 2D samples, such as thin layers, it may be advantageous to use PAs whose radiation characteristics extend over a broader area at the expense of the maximum field enhancement, as the filling factor will be better. On the other hand, for nanostructured samples it will be advantageous to employ PAs that provide high field enhancements in a localized area. 6) Use of reflectors: if the experimental setup allows it, a back reflector placed at a suitable distance from the PA array, e.g., on the back

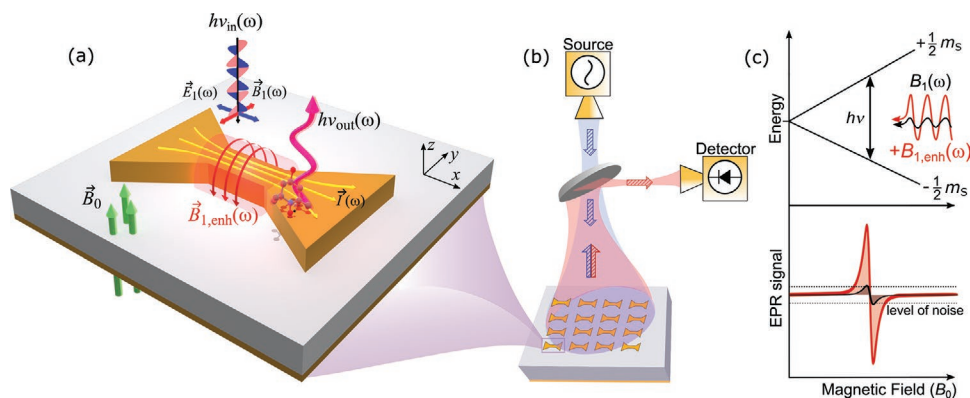


Figure 1. a) Overview of the operating principle of the plasmonic metasurface resonator during a magnetic resonance experiment. The electric field component (E_1) of the incident THz radiation ($h\nu_{in}$) excites the antenna causing a locally enhanced THz magnetic field ($B_{1,enh}$) oriented around the antenna's bridge. The enhanced THz magnetic field ($B_{1,enh}$), together with the THz magnetic field component (B_1), is absorbed by the sample placed on top of the antenna. b) Simplified scheme of the EPR setup (see also the Experimental Section). c) An EPR signal is detected at the molecular spin resonance, i.e., when the frequency of the radiation matches the energy difference of the spin levels of the molecule. The energy splitting of the spin levels depends on the static magnetic field that is applied (B_0). In a typical EPR experiment, the magnetic field is swept and the frequency is kept constant. The EPR signal that is detected is proportional to the square of the THz magnetic field.

of the substrate where the PAs are fabricated, may dramatically increase the antenna gain (see below).

We have used diablo-shaped PAs as constituent units of our PMR, because the THz magnetic field produced by the PA, $B_{1,enh}$, is oriented in a circular fashion around the PA's bridge. The polarization directly above the central part of the bridge (where the sample is) is thus mainly oriented parallel to the array plane and therefore perpendicular to the B_0 of the magnet employed here. In addition, diablo PAs can be activated or deactivated by rotating the polarization of the incoming THz electric field with respect to the long axis of the antenna: only when both are parallel will a resonant response be produced. This switching is not possible for other PAs, such as split-ring resonators. Furthermore, the latter feature more localized magnetic field enhancements, which, however, are normal to the PA and thus unsuitable for the present purposes. Several modifications to diablo nano-PA structures, e.g., fractal, cross-diablo, metal-insulator-metal, broken-diablo, have been reported to finely tune their resonance frequencies and bandwidths.^[49–53]

Concerning the choice of frequency, for HFEPR, resonance frequencies in the lower THz regime—hundreds of GHz—are required. This frequency is a compromise between the desire to use high radiation frequencies, leading to higher sensitivities and resolutions, and the practical limit posed by magnetic fields that can be reached with standard superconducting magnets (≈ 15 T). Although the relation between magnetic field and frequency is imposed by the electronic spin resonance and is specific for the investigated system, the spin transition of a free electron is taken as a reference: 300 GHz corresponds to 10.7 T.^[54] Plasmonic structures were designed and optimized by extensive numerical simulations using CST Microwave Studio (see the Experimental Section).

2.2. Numerical Simulations

All simulations employed a Gaussian beam as the source of electromagnetic radiation that is linearly polarized in the x -direction and propagates toward the $-z$ -direction, i.e., normal to the xy

plane of the PMR (xyz frame as defined in Figure 1). The PAs were designed using gold as a material, given its good plasmonic properties and its high stability, while quartz was selected as the material for the substrate, given its low dielectric losses in the THz range. Materials such as silicon or sapphire have similar low losses in this frequency region; therefore, they should also support strong plasmonic resonances and could be used instead of quartz. However, these materials often possess higher levels of impurities that exhibit EPR signals. The near-field discussed in the following is always determined by averaging the in-plane magnetic field component over an area corresponding to the central antenna, at a 10 nm height above this. First, we optimized the geometric parameters of a single diablo PA to give the maximum magnetic field enhancement in the antenna near-field. The calculated relative THz magnetic near-field, obtained after dividing by the average magnetic field of the radiation source, is shown in Figure 2a as a function of frequency. The PA response displays a broad maximum at 270 GHz with an enhancement factor of 22 and a full-width at half-maximum (FWHM) of 90 GHz. To increase the area over which the HFEPR intensity is enhanced, we moved to an array of diablo PAs that each have the same geometric dimensions as the individual PA.

We chose a 7×7 square array as this corresponds to the structure that was eventually realized. Simulations performed on smaller (3×3 and 5×5) and larger (9×9) arrays show superimposable results (Figure S1, Supporting Information). The near-field response of the array (Figure 2a) is similar to the single antenna response, but the enhancement is slightly higher (a factor of 26 instead of 22) and is almost constant between 252 and 318 GHz. This suggests that the antennas interact with each other in some way. While only a slight increase of the enhancement occurs, the overall field enhancement above the array is much larger on account of the larger active volume provided by having 49 antennas rather than one.

Our HFEPR spectrometer is a double-pass transmission setup, which features a mirror behind the sample that reflects the radiation and sends it through the sample a second time. To simulate this, we included a gold layer on the back of the antenna substrate in our simulations. As a result, the response

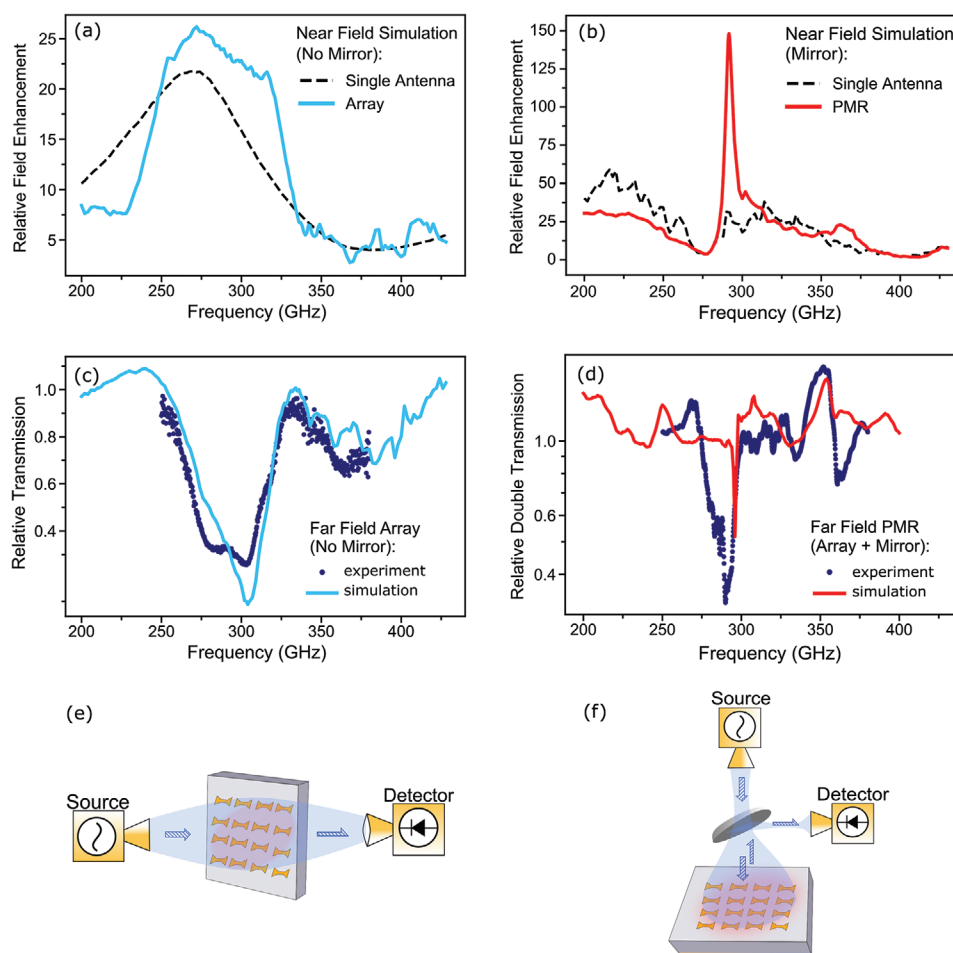


Figure 2. a,b) Simulated frequency dependence of the in-plane components of the magnetic near-field for a single diablo antenna and the array a) without and b) with a gold mirror layer on the back of the substrate. All the models include the quartz substrate. The resulting amplitudes are divided by the average in-plane magnetic field strength of the Gaussian beam source. c) Comparison of THz transmission experiment and simulation of the far-field ratios for the array without gold layer. d) Comparison of THz double-transmission experiment and simulation of the far-field ratios for the array with gold layer (PMR). The ratios are taken by dividing the active (incident electric field along the x -direction) and nonactive (incident electric field along the y -direction) signal. e,f) Simplified scheme of the e) THz transmission and f) THz double transmission experiments (more details in the Experimental Section).

changes completely (Figure 2b). The frequency dependence of the single antenna resonance exhibits two bands with stronger relative field enhancement, i.e., 60 at 216 GHz and 37 at 328 GHz. Moving to the array, the response when including the gold layer is now much sharper compared to the other configurations, with a maximum relative field enhancement of 150 at 291.5 GHz. The quality (Q)-factor, $Q = f/\Delta f$, i.e., the ratio between the resonance frequency (f) and the bandwidth determined at the FWHM, (Δf), is 40 for the final PMR model (Figure 2b), while it is between 2 and 4 in the other three cases (Figure S2, Supporting Information). This is a remarkably high value when compared to other plasmonic metamaterials, where Q usually does not exceed 10.^[55,56] Inspection of the simulated field distribution reveals that, besides the plasmonic effects, the array works as a 2D grid. This produces Fabry–Pérot oscillations of the THz radiation within the quartz substrate. Interference between the plasmonic resonance of the antennas and the standing waves in the substrate determines the final response of the metasurface. The amount of energy trapped in the sub-

strate is increased by enhancing the reflectivity of the substrate faces, i.e., when the gold layer is included on the bottom of the substrate. This strengthens the Fabry–Pérot resonance and therefore the total response of the PMR, which results in the high- Q response visible in Figure 2b (more detail in Figure S1, Supporting Information). By optimizing either the resonance frequency of the antenna or the substrate thickness, a maximally constructive effect was obtained. Thus, the final model of the PMR, which was used to fabricate antennas for characterization and HFEPR measurements, is composed of an array of diablo PAs combined with a reflective back surface of the substrate (Figure 3a). From this investigation, it is evident that every element plays a role in determining the final response of the PMR. The resonance of the modeled PMR occurs at 291.5 GHz and near-field distribution maps for the magnetic and electric fields at the resonant frequency are shown in Figure 3b,d,c,e, respectively. The antennas' active mode is a longitudinal dipole type: The electric field is enhanced at the lateral wings of the antennas, whereas the magnetic field is concentrated where

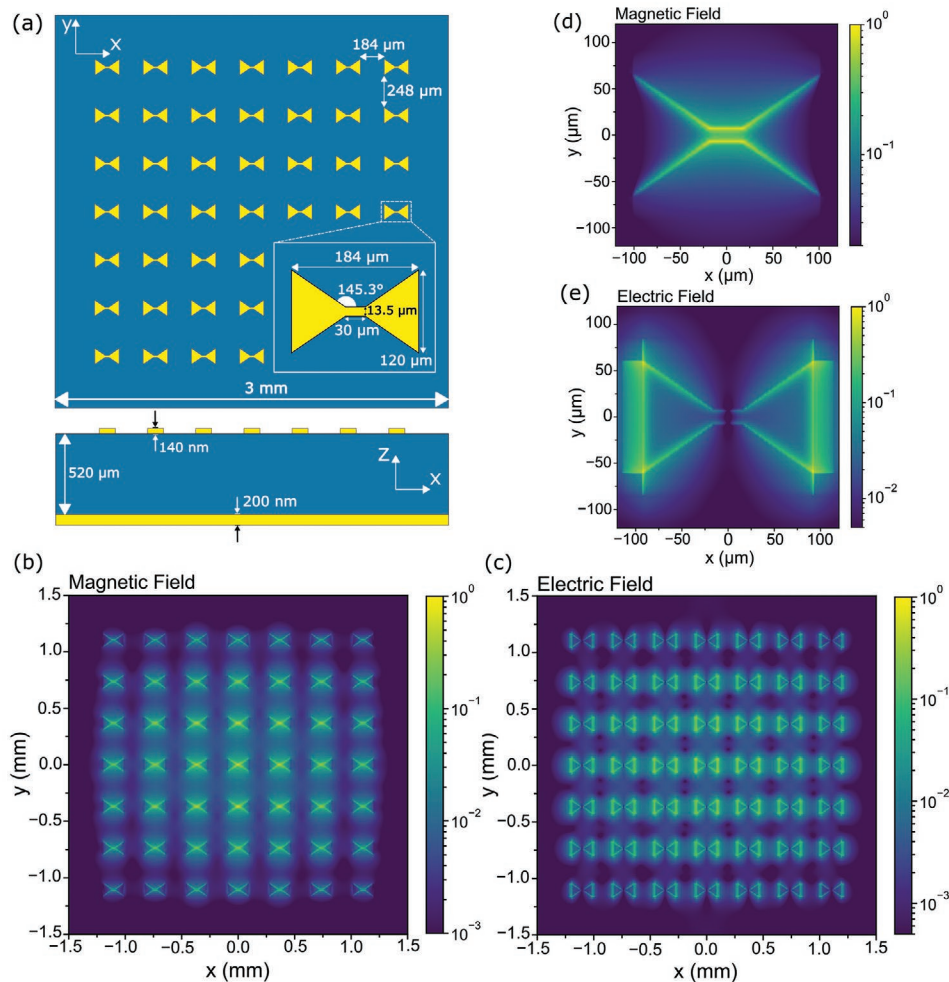


Figure 3. a) Schematic top and side views of the resonator used for modeling. The inset shows in detail the geometric parameters of the antennas. The antennas and the mirror on the back of the substrate are made of gold, while the substrate is quartz. b,c) Maps of the simulated b) magnetic and c) electric near-fields for the PMR at 291.5 GHz. d,e) An enhanced zoom of the central antenna is provided for the d) magnetic and e) electric near-fields. The maps are taken in the xy plane 10 nm above the antennas' plane. The electric field component (polarization) of the Gaussian beam is oriented along the x -axis. The amplitude of THz field enhancement follows the amplitude profile of the Gaussian beam. All maps are normalized to the maximum field value.

the current density is highest (Figure S3, Supporting Information), i.e., across the bridge connecting the two wings.^[57] As a further feature of the diabolos antennas, the resonance occurs when the polarization of the incident electric field is parallel to the antenna length (x -direction), as confirmed by simulations (Figure S4, Supporting Information). We can therefore define active and nonactive orientations corresponding to the electric field vector parallel to the x - and y -directions, respectively.

2.3. Terahertz Transmission Experiments

The designed PMR was fabricated by electron beam lithography (see the Experimental Section) and characterized by means of room temperature THz transmission (Figure 2c) and double-pass transmission (Figure 2d) experiments. Indeed, we cannot measure the far-field transmission through a single antenna, as the aperture would have to be smaller than the wavelength. However, we can measure the transmission through an array

of antennas and the double-pass transmission through an array with a back reflector—the PMR. The transmission experiment was performed in the frequency range of 250–380 GHz, and the result for the active orientation was divided by that for the nonactive orientation of the PAs. This is necessary to remove background contributions from the measurement, including effects of standing waves in the transmitted and returned beam paths. To allow for comparison with experimental results, the same approach was followed for the simulations, which is shown in Figure 2c. The experimental curve exhibits two minima at 280 and 303 GHz, which can be interpreted as a single resonance with some structuring feature. The agreement between simulation, for which no empirical parameters are used, and experiment is excellent. Not only is the transmission minimum found exactly where it is predicted by simulation, the latter also reproduces finer details, such as the slight structuring of the main resonance as well as a smaller minimum at ≈ 360 GHz. The double-pass transmission experiment was carried out in the same frequency range and, once more, the

results were obtained by dividing active to nonactive orientation signals to remove background contributions. The returned THz radiation, which is co-polar with the incident radiation, was recorded and is shown in Figure 2d together with the simulation result. The theoretical resonance peak is at 296 GHz and is very sharp. The experimental resonance peak lies at slightly lower frequency and is broader, which can be attributed to the presence of parasitic losses at the sample position or through the optical co-polar path. Interestingly, the features outside the resonance region, e.g., at 355 GHz, are also largely reproduced by the simulation.

2.4. High-Frequency EPR Experiments

Having characterized the PMR, we now turn to the application in HFEPFR measurements. To this end, we prepared a thin film of 4-hydroxy-2,2,6,6-tetramethylpiperidine-1-oxyl (TEMPO) radical diluted 1:20 (by weight) in a poly(methyl methacrylate) (PMMA) matrix deposited by spin-coating on top of the PMR. A second sample was prepared by spin-coating on top of a bare quartz substrate. These samples are hereafter indicated by $\mathbf{1}_{\text{PMR}}$ and $\mathbf{1}_{\text{REF}}$, respectively. The thickness of the films was determined by profilometry to be 330 ± 10 nm. Field-frequency magnetic resonance (FFMR) maps were measured between 250 and 370 GHz and from 8.3 to 13.3 T at a fixed temperature of 10 K. Furthermore, both the active ($\mathbf{1}_{\text{PMR-ACT}}$) and nonactive ($\mathbf{1}_{\text{PMR-NA}}$) orientations of the PMR were investigated to disentangle the antenna contribution from the total response. The signal processing of the raw FFMR maps (Figures S5–S7, Supporting Information) consisted of subtracting the standing waves, fitting the EPR signal as a function of frequency by a Gaussian derivative line-shape function and integrating the latter (see the Experimental Section). The resulting FFMR map is shown in Figure 4a for $\mathbf{1}_{\text{PMR-ACT}}$, Figure S8 in the Supporting Information for $\mathbf{1}_{\text{PMR-NA}}$, and Figure S9 in the Supporting Information for $\mathbf{1}_{\text{REF}}$. In all cases, the signal corresponds to the diagonal line in the map and it comes from the magnetic resonance excitation of the TEMPO electronic spins, which have $S = 1/2$ (see also Figure 1c). The observed signal is described by the Zeeman splitting $\Delta E = g\mu_B B_0$ of the TEMPO electron spin, where μ_B is the Bohr magneton constant and the g -factor is $2.0072(1)$.^[54] While the map provides a useful overview, the EPR signal is more clearly visualized by plotting the signal intensity along the diagonal as a function of either the magnetic field or frequency. The latter is shown in Figure 4b. The signal of $\mathbf{1}_{\text{REF}}$ is frequency dependent and displays maxima at ≈ 275 and 320 GHz. Moreover, small oscillations are visible across the spectrum. These intensity variations are mainly the result of standing waves within the quasi-optical path, which lead to oscillations in the detected intensity.^[54] It is worth underlining the oscillation period of 3.3 GHz in the frequency domain, corresponding to 4.5 cm between reflecting elements, which is equal to the length of the smooth waveguide taper connected to the corrugated waveguide. In contrast, the source intensity is largely featureless, dropping off slightly at the band edges.^[54] Compared to $\mathbf{1}_{\text{REF}}$, the sample $\mathbf{1}_{\text{PMR-NA}}$ features a wide nonresonant broad signal enhancement between 285 and 365 GHz, indicating that the PMR influences the signal even when the PAs are not

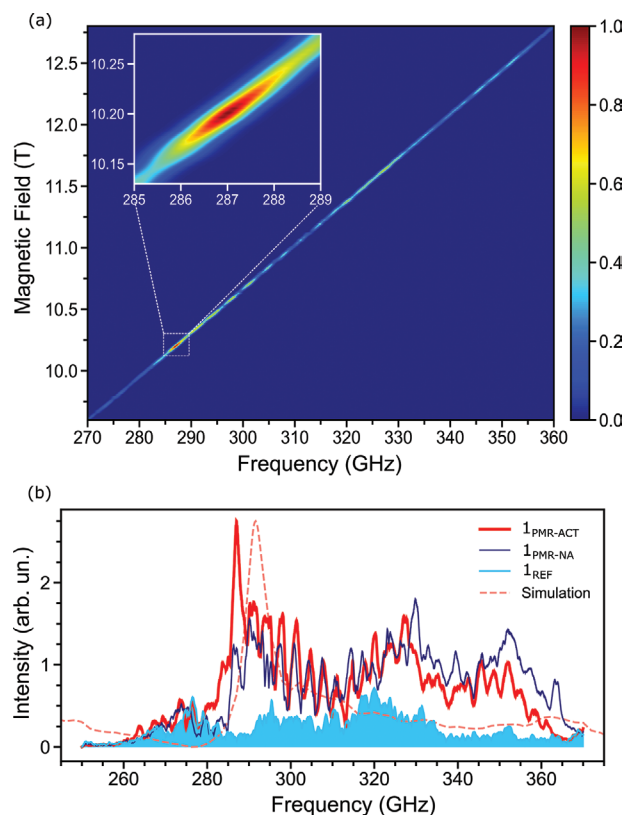


Figure 4. a) FFMR map measured in HFEPFR for $\mathbf{1}_{\text{PMR}}$ in the active orientation at 10 K; the PMR resonance area is highlighted in the inset. The color scale is linear and normalized to unity. b) Comparison of the frequency profiles extracted by the experimental FFMR maps for the PMR in the active ($\mathbf{1}_{\text{PMR-ACT}}$), nonactive ($\mathbf{1}_{\text{PMR-NA}}$) orientations and for the reference sample constituted by bare quartz ($\mathbf{1}_{\text{REF}}$). The simulation of the PMR near-field shown in Figure 2b is here reported, and its intensity is scaled for comparison.

active. Furthermore, the 3.3 GHz oscillations are more accentuated here. The signal of $\mathbf{1}_{\text{PMR-ACT}}$ is overall similar to that of $\mathbf{1}_{\text{PMR-NA}}$, but with the addition of a narrow-band resonant intensity enhancement at 287 GHz (inset of Figure 4a). The position and shape of this peak match well with the PMR resonance at 291.5 GHz observed in the near-field simulation for the active position of the antennas, which is overlaid in Figure 4b for convenience. This indicates that the signal enhancement in the narrow band at 287 GHz occurs because of the plasmonic enhancement of the THz magnetic field induced by the PMR.

3. Discussion

The signal enhancement produced by the PMR can be estimated using $\mathbf{1}_{\text{REF}}$ as a reference. For both $\mathbf{1}_{\text{PMR-ACT}}$ and $\mathbf{1}_{\text{PMR-NA}}$, a signal enhancement between 5 and 10 occurs in the broad frequency range from 280 to 365 GHz (Figure 4b). Unlike in the THz transmission measurements, in the current HFEPFR experiments, deviations from a parallel orientation between the PMR and the polarization of the incident radiation are more likely to occur due to experimental limitations. This would agree with the signal enhancement that is still observed for $\mathbf{1}_{\text{PMR-NA}}$, which

is oriented at 90° from $\mathbf{1}_{\text{PMR-ACT}}$. The reason enhancements are observed over such a broad THz frequency range, evident in both cases, originates from the Fabry–Pérot interference within the dielectric substrate induced by the array on one side and the gold layer on the other. The strongest enhancement, by a factor of ≈ 30 with respect to $\mathbf{1}_{\text{REF}}$, occurs for the active antenna orientation at the PMR resonance (287 GHz), meaning that employing the PMR has led to a 30-fold increase of the EPR signal intensity. Through numerical simulations, it is also possible to calculate the magnitude of the signal enhancement and compare it to the experimental results. To this end, the square of the magnetic near-field was averaged considering the same volume of the experimental sample placed over the entire array, i.e., $3 \text{ mm} \times 3 \text{ mm} \times 330 \text{ nm}$ volume above the PMR model, $\langle H_{\text{PMR}}^2 \rangle$. The same was repeated for the reference sample taking as a model the quartz substrate without PAs and with gold coating on the back, $\langle H_{\text{REF}}^2 \rangle$. The enhancement is then calculated by taking the ratio $\langle H_{\text{PMR}}^2 \rangle / \langle H_{\text{REF}}^2 \rangle$ and results to be 280. The deviation between the predicted (280) and experimental (30) enhancement factors is again consistent with a nonperfect alignment of the PMR with respect to the polarization of the incident radiation. In addition, we cannot exclude further losses due to imperfections in the fabricated PMR that are not present in numerical simulations, e.g., potentially the two surfaces of the substrate are not perfectly plane-parallel.

In any case, a 30-fold enhancement factor constitutes a significant improvement when measuring thin-layer samples covering the entire substrate. It is important to emphasize averaging over the entire antenna array rather than over the hotspot of the antennas underestimates the local field enhancement. Indeed, a much higher enhancement is expected when the investigated sample is confined to the PA hotspot, e.g., if the molecules are grafted directly to the gold antennas of the PMR. For such a scenario, we evaluated the effect of the PMR by numerical simulations. In this case, the square magnetic near-field is integrated over only the antenna area, i.e., in a diaboloid-like area. The ratio $\langle H_{\text{PMR}}^2 \rangle / \langle H_{\text{REF}}^2 \rangle$ results in a factor of 7500, i.e., 26 times higher than what is calculated when averaging over the entire sample volume. The minimum number of detectable spins (*mnds*) can be estimated by analyzing the experimental signal-to-noise ratio (*S/N*) of the FFMR maps. By extrapolating the *S/N* to 1 for $\mathbf{1}_{\text{REF}}$, we obtain an *mnds* of $\approx 10^{10}$ spins $(\text{G Hz}^{1/2})^{-1}$ at 10 K and 287 GHz, which agrees with what was previously obtained.^[54] By repeating the same analysis on the FFMR map of $\mathbf{1}_{\text{PMR-ACT}}$, we found an *mnds* of $\approx 10^9$ spins $(\text{G Hz}^{1/2})^{-1}$ at 10 K and 287 GHz. In this case, the volume of the measured thin film was $3 \text{ mm} \times 3 \text{ mm} \times 330 \text{ nm}$, i.e., the layer covering the entire substrate. On the other hand, if the sample is addressed directly on the gold antennas of the PMR, the estimated *mnds* decreases to $\approx 10^6$ spins $(\text{G Hz}^{1/2})^{-1}$ at 10 K at the PMR resonance frequency. In comparison, the number of spins for a monolayer with a hypothetical density of 1 spin nm^{-2} covering only the $10^4 \mu\text{m}^2$ PA hotspot area and considering the 49 PAs of the PMR, is $\approx 5 \times 10^{11}$ spins. With the estimated *mnds* of $\approx 10^6$ spins $(\text{G Hz}^{1/2})^{-1}$ at 10 K, this leads to an *S/N* ratio of over 10^5 . Therefore, the gain in sensitivity provided by the PMR would allow measuring HFEP spectra of monolayer samples with the same spectral quality that would be obtained for bulk samples. To contextualize these results, state-of-the-art detection

limits for HFEP spectrometers are usually between 10^{10} and 10^9 spins $(\text{G Hz}^{1/2})^{-1}$ *mnds* at high frequency and low temperature. Furthermore, there are two main points to consider. First, there is an inherent relationship between resonator and type of sample. Because different resonators provide different distributions of electromagnetic fields, their performances will depend on the sample form, i.e., solution, powder, thin layer, or crystal. Differently from all other types of resonator, the PMR concentrates the field strength in a 2D volume and therefore it manifests high performances specifically for thin-film and monolayer samples. Second, plasmonic resonances strengthen as the frequency is increased. Therefore, the performances of metasurfaces, in terms of signal enhancement, are expected to increase accordingly. This can help to counteract the signal reduction occurring at higher frequencies due to technological limits of THz sources. Eventually, the high tunability of metasurface-based resonators make them adaptable to a large variety of setups and potentially to other type of samples.

4. Conclusion

We have proposed a novel type of plasmonic metasurface resonator, based on an array of gold diaboloid antennas in combination with a back reflector, to use in HFEP spectroscopy. The push for higher frequencies (above 100 GHz) in HFEP is motivated by the improved spectral resolution, as well as the ability to access integer spin systems that are otherwise silent or difficult to interpret at standard EPR frequencies. We have found both nonresonant broadband and resonant narrowband EPR signal enhancements due to the PMR. The latter is a factor of 30. Local hotspot signal enhancement is predicted to reach a factor of 7500, leading to a potential minimum number of detectable spins of $\approx 10^6$ spins $(\text{G Hz}^{1/2})^{-1}$ at low temperatures. This potentially opens HFEP to the investigation of self-assembled monolayer samples, thin-layer samples as well as limited-volume biological samples. Moreover, this paves the way for the development of new strategies to integrate molecules in circuits based on plasmonic metasurfaces working in the THz frequency range.^[58–61] Further improvements in antenna design, based on a more in-depth understanding of their coupling, the interplay with substrate modes, and the possibility of integrating an external active control, are expected to further increase the sensitivity enhancement and enlarge their applicability range.^[62,63] Given the high flexibility and the ease of fabrication, we envisage that more plasmonic metasurface resonators will be designed and customized for different applications in magnetic resonance techniques working at high frequencies.

5. Experimental Section

Simulations: Numerical simulations were carried out by using CST Microwave Studio software (Dassault Systèmes) with the Time Domain Solver. A linearly polarized Gaussian beam with a radius of 1.5 mm was used as a source. The simulated frequencies range between 200 and 450 GHz with step-sizes of 1 GHz, decreased to 0.5 GHz around the resonance. Appropriate mesh sizes were used for computing the fields in the antenna and mirror regions. The electric and magnetic

fields were calculated in specific areas and/or volumes as a function of the frequencies. The near-field intensities were determined 10 nm above the antenna top plane. The material parameters employed for the quartz substrate were: dielectric constant $\epsilon = 4.4$ and loss tangent $\delta = 0.0001$, according to ref. [64]. For the PMR, the model studied was the entire metasurface resonator composed of quartz substrate with the 7×7 diablo antennas array on one side and a gold layer on the opposite side. For the array, the model consisted of the 7×7 diablo antenna array on the quartz substrate without a gold layer. For the single antenna, the model consisted of a single diablo antenna on a quartz substrate. The single antenna response was also simulated including the gold layer. In all cases, the magnetic near-field was calculated as the average of the in-plane magnetic field component over the entire area (diabolo-like shape) of the central antenna. The experimental choice of a 7×7 antenna array was determined by the limited diameter of the HFEPR sample holder.

Fabrication: The antenna array was fabricated by using standard electron beam lithography (Raith eLine Plus) in a double layer positive tone resist (PMMA), 200K and 950K type, Allresist) on a quartz substrate (CrysTec GmbH, z-cut, orientation (0001), both sides polished). After development, a 2 nm chromium adhesion and a 140 nm gold layer were deposited via electron-beam evaporation. All dimensions are depicted in Figure 3a.

Sample Preparation: For the chemical sample preparation, 4-hydroxy-2,2,6,6-tetramethylpiperidine-1-oxyl (assay $\geq 98\%$) was purchased from Fluka Analytical, while PMMA was purchased from Sigma Aldrich (MW $\approx 350\,000$ by GPC, density: 1.17 g mL^{-1}). Separate chlorobenzene solutions were prepared of 50 g L^{-1} of TEMPOL and 70 g L^{-1} of PMMA. The solutions were mixed to obtain a 5% of TEMPOL in a 50 g L^{-1} of PMMA solution immediately prior to the deposition on the substrate by spin-coating. The substrates (PMR and bare quartz) were cleaned a) in an ultrasonic bath using isopropanol and then acetone and b) using a CO_2 stream (Applied Surface Technologies SnowJet) while heating the substrate to $100\text{ }^\circ\text{C}$. The films were prepared by static spin-coating with a rotation rate of 2000 rpm for 1 min (Ramgrabber). The thickness was estimated by profilometry (Dektak Stylus Profiler, Bruker).

Single-Pass Transmission Measurements: These were carried out using a custom built quasi-optical measurement bench consisting of a THz source and zero-bias detector, as well as elliptical mirrors for focusing the radiation. The source was used in continuous-wave mode. The sample holder featured an aperture diameter of 2.5 cm to counter parasitic radiation and allowed in situ rotations of the antenna array (Figure S10, Supporting Information).

Double-Pass Transmission Measurements: They were performed with the sample placed inside the cryostat kept at $T = 150\text{ K}$ and exploiting a home-built HFEPR setup (Figure S11, Supporting Information).^[54] We detected the co-polar component of the reflected radiation by means of a zero-bias detector. All measurements were performed with the antenna arrays in active and nonactive orientations and the ratio between these two orientations was taken.

High-Frequency EPR Measurements: These were carried out on a home-built spectrometer that was previously described (Figure S11, Supporting Information).^[54] The FFMR maps were measured with a field modulation amplitude of 3 mT and a field modulation frequency of 30 kHz, while the time constant of the lock-in amplifier was set to 3 ms. The THz radiation frequency was swept with 1 s per scan, while the magnetic field was continuously swept with a rate of 0.01 T s^{-1} . The measurements were carried out in induction mode,^[65] i.e., the component of the reflected radiation orthogonal to the incident radiation was recorded. Data analyses were carried out in Python using NumPy, SciPy, and Matplotlib libraries.^[66–68] The measured signal was processed in the following steps: 1) correction of the phase shift between the x/y channels of the lock-in amplifier; 2) partial subtraction of the standing waves; 3) fit of the individual curves with a Gaussian derivative model; 4) integration of the fitted curves. This procedure was applied for multiple purposes: correct the microwave phase, remove background noise for integration, and display the signal as an absorption peak instead of the first derivative. This allowed for an easier and more reliable visualization of maps and profiles.

Supporting Information

Supporting Information is available from the Wiley Online Library or from the author.

Acknowledgements

This research has been supported by European Union's Horizon 2020 programme FET-OPEN project PETER, GA 767 227. The Center for Integrated Quantum Science and Technology (IQST), and the Carl Zeiss Foundation are also acknowledged. The authors thank Brno University of Technology (FSI-S-20-6485) and the GAČR project 20–28573S. The authors acknowledge financial support from the Spanish Ministry of Science, Innovation and Universities (national project RTI2018-094830-B-I00 and the project MDM-2016-0618 of the Maria de Maeztu Units of Excellence Program) and the Basque Government (grant No. IT1164-19). The authors thank Prof. Sabine Ludwigs and David Neusser for access to the SnowJet cleaner. The authors thank Thomas Keating Ltd. for providing the quasi-optical bench used for the transmission measurements of the PMR. The authors thank Dennis Schäfer for the valuable support provided for the Python scripts and Martin Konečný for useful discussions.

Open access funding enabled and organized by Projekt DEAL.

Conflict of Interest

The authors declare no conflict of interest.

Data Availability Statement

The data that support the findings of this study are available from the corresponding authors upon reasonable request.

Keywords

2D resonators, electron paramagnetic resonance, nanostructures, plasmonic metasurfaces, self-assembled monolayers, spintronics, thin layers

Received: April 8, 2021

Revised: June 28, 2021

Published online: July 29, 2021

- [1] O. Grinberg, L. J. Berliner, *Very High Frequency (VHF) ESR/EPR*, Vol. 22, Springer Science+Business Media, LLC, New York **2004**.
- [2] J. A. Weil, J. R. Bolton, *Electron Paramagnetic Resonance: Elementary Theory and Practical Applications*, John Wiley & Sons, Inc., New York **2006**.
- [3] E. J. Reijerse, *Appl. Magn. Reson.* **2010**, *37*, 795.
- [4] A. Sojka, M. Šedivý, O. Laguta, A. Marko, V. T. Santana, P. Neugebauer, in *Electron Paramagnetic Resonance*, Vol. 27 (Eds: V. Chechik, D. M. Murphy, B. E. Bode), Royal Society of Chemistry, London **2021**, pp. 214.
- [5] D. M. Mittleman, *Nat. Photonics* **2013**, *7*, 666.
- [6] D. M. Mittleman, *J. Appl. Phys.* **2017**, *122*, 230901.
- [7] S. Milikisiyants, A. A. Nevzorov, A. I. Smirnov, *J. Magn. Reson.* **2018**, *296*, 152.
- [8] D. Marsh, *Spin-Label Electron Paramagnetic Resonance*, CRC Press, Boca Raton, FL **2020**.

- [9] J. P. Campbell, J. T. Ryan, P. R. Shrestha, Z. Liu, C. Vaz, J.-H. Kim, V. Georgiou, K. P. Cheung, *Anal. Chem.* **2015**, *87*, 4910.
- [10] M. Lucarini, L. Pasquato, *Nanoscale* **2010**, *2*, 668.
- [11] D. Gatteschi, R. Sessoli, J. Villain, *Molecular Nanomagnets*, Oxford University Press, Oxford **2006**.
- [12] L. Tesi, E. Lucaccini, I. Cimatti, M. Perfetti, M. Mannini, M. Atzori, E. Morra, M. Chiesa, A. Caneschi, L. Sorace, R. Sessoli, *Chem. Sci.* **2016**, *7*, 2074.
- [13] M. Warner, S. Din, I. S. Tupitsyn, G. W. Morley, A. M. Stoneham, J. A. Gardener, Z. Wu, A. J. Fisher, S. Heutz, C. W. M. Kay, G. Aepli, *Nature* **2013**, *503*, 504.
- [14] K. Bader, D. Dengler, S. Lenz, B. Endeward, S.-D. Jiang, P. Neugebauer, J. van Slageren, *Nat. Commun.* **2014**, *5*, 5304.
- [15] M. Atzori, L. Tesi, E. Morra, M. Chiesa, L. Sorace, R. Sessoli, *J. Am. Chem. Soc.* **2016**, *138*, 2154.
- [16] G. Cucinotta, L. Poggini, A. Pedrini, F. Bertani, N. Cristiani, M. Torelli, P. Graziosi, I. Cimatti, B. Cortigiani, E. Otero, P. Ohresser, P. Saintavit, A. Dediu, E. Dalcanale, R. Sessoli, M. Mannini, *Adv. Funct. Mater.* **2017**, *27*, 1703600.
- [17] L. Bogani, W. Wernsdorfer, *Nat. Mater.* **2008**, *7*, 179.
- [18] L. Gragnaniello, F. Paschke, P. Erler, P. Schmitt, N. Barth, S. Simon, H. Brune, S. Rusponi, M. Foini, *Nano Lett.* **2017**, *17*, 7177.
- [19] M. Mannini, F. Pineider, P. Saintavit, C. Danieli, E. Otero, C. Sciancalepore, A. M. Talarico, M. A. Arrio, A. Cornia, D. Gatteschi, R. Sessoli, *Nat. Mater.* **2009**, *8*, 194.
- [20] A. Cini, M. Mannini, F. Totti, M. Fittipaldi, G. Spina, A. Chumakov, R. Ruffer, A. Cornia, R. Sessoli, *Nat. Commun.* **2018**, *9*, 480.
- [21] R. Narkowicz, D. Suter, R. Stonies, *J. Magn. Reson.* **2005**, *175*, 275.
- [22] R. Narkowicz, D. Suter, I. Niemeyer, *Rev. Sci. Instrum.* **2008**, *79*, 084702.
- [23] A. Banholzer, R. Narkowicz, C. Hassel, R. Meckenstock, S. Stienen, O. Posth, D. Suter, M. Farle, J. Lindner, *Nanotechnology* **2011**, *22*, 295713.
- [24] C. Clauss, M. Dressel, M. Scheffler, *J. Phys.: Conf. Ser.* **2015**, *592*, 012146.
- [25] H. Malissa, D. I. Schuster, A. M. Tyryshkin, A. A. Houck, S. A. Lyon, *Rev. Sci. Instrum.* **2013**, *84*, 025116.
- [26] B. Miksch, M. Dressel, M. Scheffler, *Rev. Sci. Instrum.* **2020**, *91*, 025106.
- [27] T. J. Yen, W. J. Padilla, N. Fang, D. C. Vier, D. R. Smith, J. B. Pendry, D. N. Basov, X. Zhang, *Science* **2004**, *303*, 1494.
- [28] J. B. Pendry, D. Schurig, D. R. Smith, *Science* **2006**, *312*, 1780.
- [29] D. Schurig, J. J. Mock, B. J. Justice, S. A. Cummer, J. B. Pendry, A. F. Starr, D. R. Smith, *Science* **2006**, *314*, 977.
- [30] D. R. Smith, J. B. Pendry, M. C. K. Wiltshire, *Science* **2004**, *305*, 788.
- [31] A. V. Kildishev, A. Boltasseva, V. M. Shalaev, *Science* **2013**, *339*, 1232009.
- [32] H. T. Chen, A. J. Taylor, N. F. Yu, *Rep. Prog. Phys.* **2016**, *79*, 076401.
- [33] W. Withayachumnankul, D. Abbott, *IEEE Photon. J.* **2009**, *1*, 99.
- [34] J. B. Pendry, L. Martin-Moreno, F. J. Garcia-Vidal, *Science* **2004**, *305*, 847.
- [35] F. A. A. Nugroho, D. Albinsson, T. J. Antosiewicz, C. Langhammer, *ACS Nano* **2020**, *14*, 2345.
- [36] J. Qin, L. J. Deng, T. T. Kang, L. X. Nie, H. Y. Feng, H. L. Wang, R. Yang, X. Liang, T. T. Tang, J. Shen, C. Y. Li, H. B. Wang, Y. Luo, G. Armelles, L. Bi, *ACS Nano* **2020**, *14*, 2808.
- [37] H. H. Hsiao, C. H. Chu, D. P. Tsai, *Small Methods* **2017**, *1*, 1600064.
- [38] J. A. Schuller, E. S. Barnard, W. Cai, Y. C. Jun, J. S. White, M. L. Brongersma, *Nat. Mater.* **2010**, *9*, 193.
- [39] M. D. Sonntag, J. M. Klingsporn, A. B. Zrimsek, B. Sharma, L. K. Ruvuna, R. P. Van Duyne, *Chem. Soc. Rev.* **2014**, *43*, 1230.
- [40] J. Gao, N. Zhang, D. X. Ji, H. M. Song, Y. H. Liu, L. Zhou, Z. Sun, J. M. Jornet, C. Thompson, R. L. Collins, Y. Song, S. H. Jiang, Q. Q. Gan, *Small Methods* **2018**, *2*, 1800045.
- [41] M. Bauch, K. Toma, M. Toma, Q. Zhang, J. Dostalek, *Plasmonics* **2014**, *9*, 781.
- [42] W. Hou, S. B. Cronin, *Adv. Funct. Mater.* **2013**, *23*, 1612.
- [43] F. Pineider, E. Pedrueza-Villalmanzo, M. Serri, A. M. Adamu, E. Smetanina, V. Bonanni, G. Campo, L. Poggini, M. Mannini, C. D. Fernandez, C. Sangregorio, M. Gurioli, A. Dmitriev, R. Sessoli, *Mater. Horiz.* **2019**, *6*, 1148.
- [44] S. W. Zeng, K. V. Sreekanth, J. Z. Shang, T. Yu, C. K. Chen, F. Yin, D. Baillargeat, P. Coquet, H. P. Ho, A. V. Kabashin, K. T. Yong, *Adv. Mater.* **2015**, *27*, 6163.
- [45] D. Verschuere, X. Shi, C. Dekker, *Small Methods* **2019**, *3*, 1800465.
- [46] N. Maccaferri, *J. Opt. Soc. Am. B* **2019**, *36*, E112.
- [47] Z. Fusco, M. Rahmani, R. H. Bo, R. Verre, N. Motta, M. Kall, D. Neshev, A. Tricoli, *Adv. Mater.* **2018**, *30*, 1800931.
- [48] X. J. Liu, J. J. Wang, L. H. Tang, L. J. Xie, Y. B. Ying, *Adv. Funct. Mater.* **2016**, *26*, 5515.
- [49] T. Grosjean, M. Mivelle, F. I. Baida, G. W. Burr, U. C. Fischer, *Nano Lett.* **2011**, *11*, 1009.
- [50] Y. Yang, H. T. Dai, X. W. Sun, *AIP Adv.* **2014**, *4*, 017123.
- [51] H. Guo, B. Simpkins, J. D. Caldwell, J. Guo, *AIP Adv.* **2015**, *5*, 107149.
- [52] M. Mivelle, T. Grosjean, G. W. Burr, U. C. Fischer, M. F. Garcia-Parajo, *ACS Photonics* **2015**, *2*, 1071.
- [53] M. Hrtoň, A. Konečná, M. Horák, T. Šíkola, V. Křapek, *Phys. Rev. Appl.* **2020**, *13*, 054045.
- [54] P. Neugebauer, D. Bloos, R. Marx, P. Lutz, M. Kern, D. Aguilá, J. Vaverka, O. Laguta, C. Dietrich, R. Clerac, J. van Slageren, *Phys. Chem. Chem. Phys.* **2018**, *20*, 15528.
- [55] I. Al-Naib, C. Jansen, R. Singh, M. Walther, M. Koch, *IEEE Trans. Terahertz Sci. Technol.* **2013**, *3*, 772.
- [56] I. Al-Naib, W. Withayachumnankul, *J. Infrared Millim. Terahertz Waves* **2017**, *38*, 1067.
- [57] V. Křapek, A. Konečná, M. Horák, F. Ligmajer, M. Stoger-Pollach, M. Hrtoň, J. Babocký, T. Šíkola, *Nanophotonics* **2020**, *9*, 623.
- [58] S. S. Ding, Y. Tian, Y. Li, H. T. Zhang, K. Zhou, J. Y. Liu, L. Qin, X. X. Zhang, X. H. Qiu, H. L. Dong, D. B. Zhu, W. P. Hu, *ACS Nano* **2019**, *13*, 9491.
- [59] A. Kobke, F. Gutzeit, F. Rohricht, A. Schlimm, J. Grunwald, F. Tuzcek, M. Studniarek, D. Longo, F. Choueikani, E. Otero, P. Ohresser, S. Rohlf, S. Johannsen, F. Diekmann, K. Rosnagel, A. Weismann, T. Jasper-Toennies, C. Nather, R. Herges, R. Berndt, M. Gruber, *Nat. Nanotechnol.* **2020**, *15*, 18.
- [60] M. Kern, L. Tesi, D. Neusser, N. Russegger, M. Winkler, A. Allgaier, Y. M. Gross, S. Bechler, H. S. Funk, L. T. Chang, J. Schulze, S. Ludwigs, J. van Slageren, *Adv. Funct. Mater.* **2021**, *31*, 2006882.
- [61] M. Urdampilleta, S. Klayatskaya, M. Ruben, W. Wernsdorfer, *ACS Nano* **2015**, *9*, 4458.
- [62] T. Cui, B. F. Bai, H. B. Sun, *Adv. Funct. Mater.* **2019**, *29*, 1806692.
- [63] X. G. Luo, *Adv. Mater.* **2019**, *31*, 1804680.
- [64] P. F. Goldsmith, *Quasioptical Systems*, Institute of Electrical and Electronics Engineers, Inc., New York **1998**.
- [65] G. M. Smith, J. C. G. Lesurf, R. H. Mitchell, P. C. Riedi, *Rev. Sci. Instrum.* **1998**, *69*, 3924.
- [66] P. Virtanen, R. Gommers, T. E. Oliphant, M. Haberland, T. Reddy, D. Cournapeau, E. Burovski, P. Peterson, W. Weckesser, J. Bright, S. J. van der Walt, M. Brett, J. Wilson, K. J. Millman, N. Mayorov, A. R. J. Nelson, E. Jones, R. Kern, E. Larson, C. J. Carey, İ. Polat, Y. Feng, E. W. Moore, J. VanderPlas, D. Laxalde, J. Perktold, R. Cimrman, I. Henriksen, E. A. Quintero, C. R. Harris, et al., *Nat. Methods* **2020**, *17*, 261.
- [67] S. van der Walt, S. C. Colbert, G. Varoquaux, *Comp. Sci. Eng.* **2011**, *13*, 22.
- [68] J. D. Hunter, *Comp. Sci. Eng.* **2007**, *9*, 90.